Materials Today Bio 31 (2025) 101541

Contents lists available at ScienceDirect

Materials Today Bio

journal homepage: www.journals.elsevier.com/materials-today-bio

Curcumin-enhanced NIR-II-responsive gold nanobipyramids for targeted HSP 90 inhibition

Zhenying Diao [a,b,1], Youcheng Liang [c,1], Yong Liu [a,b,1], Dou Zhang [a,b], Long Qiu [a,b], Jianbo Sun [a], Qiaoyou Lu [a,b], Yanlei Liu [a,d,**], Daxiang Cui [a,d,***], Ting Yin [a,b,*]

[a] Research Center of Nano Technology and Application Engineering, The First Dongguan Affiliated Hospital, School of Pharmacy, Guangdong Medical University, Dongguan, 523808, Guangdong, PR China
[b] Dongguan Research Center for Biomedical Nano Engineering Technology Research, Guangdong Medical University, Dongguan, 523808, Guangdong, PR China
[c] Science and Technology Innovation Center, Guangzhou University of Chinese Medicine, Guangzhou, 510405, Guangdong, PR China
[d] School of Sensing Science and Engineering, School of Electronic Information and Electrical Engineering, Shanghai Jiao Tong University, 800 Dongchuan Road, Shanghai, 200240, PR China

ARTICLE INFO

Keywords:
Heat shock protein 90 blockade
Bioinformatic prediction
NIR-II-Responsive gold nanobipyramids
Mild PTT
Synergistic therapies

ABSTRACT

Blockade of heat shock protein 90 (HSP90) expression in multimodal synergistic therapy has a great prospect for cancer treatment. Nanomaterials combined with bioinformatic analysis provides accurate guidance for the design of anti-HSP90 nanomedicines. Herein, a NIR-II-responsive nanoplatform was developed under bioinformatics guided to effectly inhibit HSP90 for enhanced synergistic mild-photothermal chemotherapy without any notable tissue damage. The nanoplatforms were assembled from NIR-II-responsive gold nanobipyramids (GNBs) combined with curcumin (Cur) *via* hydrophobic-hydrophobic interactions and hydrogen bonds. On the basis of drug discovery and network pharmacology, we found that Cur has impressive anti-HSP90 capability and analyzed its therapeutic mechanism against NSCLC. Under the irradiation of NIR-II light, the obtained GNBs-Cur blocked the expression of HPS90 and inhibited related antiapoptotic pathways, thus enhancing the mild PTT of GNBs under 1064 nm laser irradiation. Meanwhile, Cur served as chemotherapeutic agents to induce apoptosis in tumor cells. In vivo photoacoustic imaging-guided, GNBs-Cur achieved effective tumor elimination through mild-photothermal chemotherapy without systemic toxicity. Overall, this work provides a new therapeutic modality paradigm for potential NSCLC treatment on the basis of synergistic therapies.

1. Introduction

Photothermal therapy (PTT) has emerged as an efficient cancer treatment strategy because of its spatiotemporal controllability, non-invasiveness, and low side effects [1–3]. In the PTT process, photothermal agents (PTAs) can "burn" tumor cells by generating localized heat therapy under near-infrared (NIR) light irradiation [4–6]. Owing to their excellent photothermal conversion properties and Raman scattering imaging capabilities, gold nanobipyramids (GNBs) have been used as PTAs for visualized PTT [7,8]. Li et al. developed GNB-based nanotheranostic agents for dual-modality imaging (fluorescence/photoacoustic (PA) imaging) and PTT in melanoma cancer [9]. Zhang et al. reported that GNB-based nanoprobes could trigger significant thermotherapeutic disruption with remarkable PTT efficiency (71.8 %) [10]. However, there are many hurdles that hinder the clinical application of GNBs. For example, most reported GNBs are excited by

* Corresponding author. Research Center of Nano Technology and Application Engineering, The First Dongguan Affiliated Hospital, School of Pharmacy, Guangdong Medical University, Dongguan, 523808, Guangdong, PR China.
** Corresponding author. Dongguan Research Center for Biomedical Nano Engineering Technology Research, Guangdong Medical University, Dongguan, 523808, Guangdong, PR China.
*** Corresponding author. Research Center of Nano Technology and Application Engineering, The First Dongguan Affiliated Hospital, School of Pharmacy, Guangdong Medical University, Dongguan, 523808, Guangdong, PR China.
E-mail addresses: liuyanlei@sjtu.edu.cn (Y. Liu), dxcui@sjtu.edu.cn (D. Cui), ting.yin@gdmu.edu.cn (T. Yin).
[1] These authors contributed equally to this work.

https://doi.org/10.1016/j.mtbio.2025.101541
Received 22 November 2024; Received in revised form 26 January 2025; Accepted 1 February 2025
Available online 1 February 2025

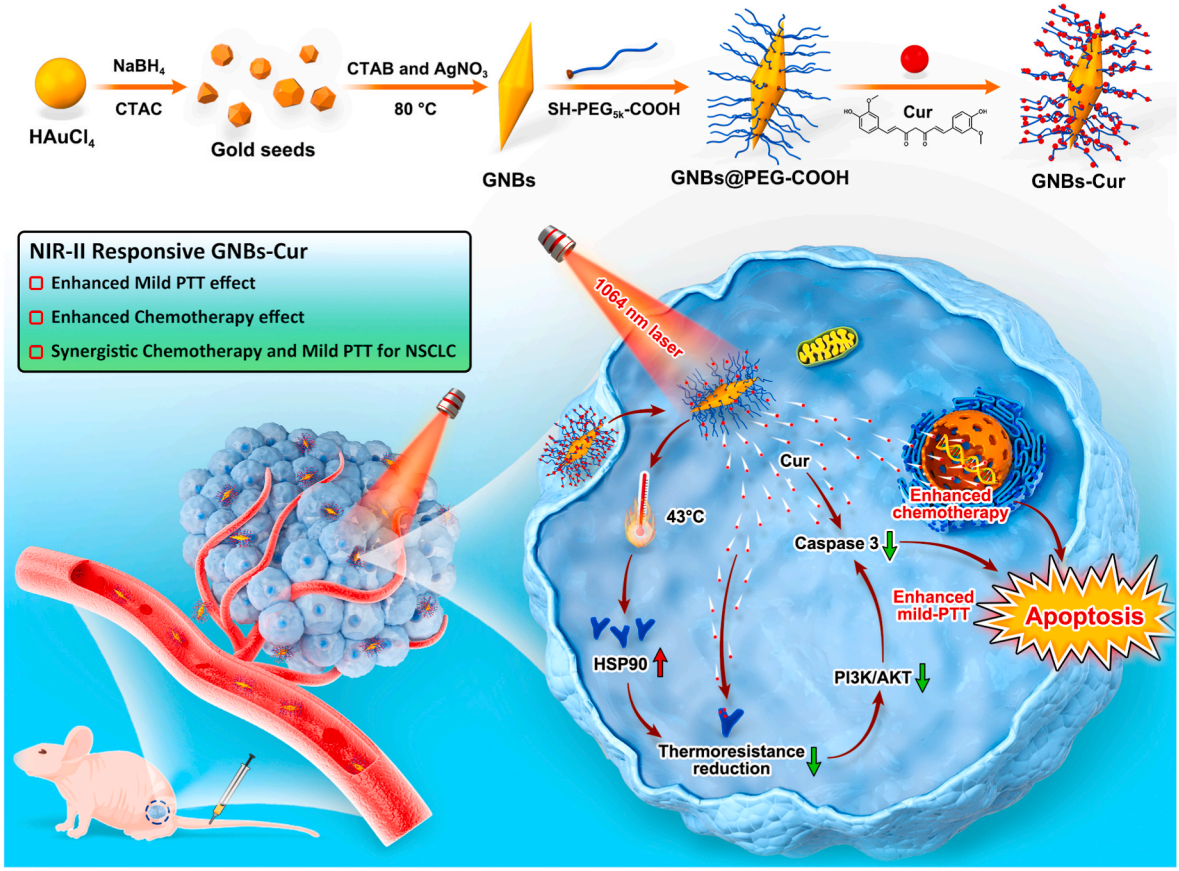

Scheme 1. Schematic showing the preparation and mechanism of GNBs-Cur. Illustration of the fabrication process of GNBs-Cur and the inhibitory effect of Cur on heat shock protein 90 (HSP90) to enhance synergistic NIR-II-guided mild PTT and chemotherapy for NSCLC.

the first NIR light window (NIR-I: 700–900 nm). Additionally, poor tissue penetration (<1 cm) of NIR-I is an important limitation of PTT [11]. In contrast to NIR-I light, the NIR-II window (NIR-II: 1000–1700 nm) exhibited diminished tissue absorption and increased tissue penetration capabilities, which has attracted extensive attention [12–14]. Furthermore, tumor cells can trigger activation of heat shock proteins (HSPs) under hyperthermia, resulting in severe thermotolerance [15–17]. HSP90, a key factor in thermotolerance, can activate many cancer-related pathways, leading to potent anti-apoptotic effects [18, 19]. Therefore, it is commonly necessary to maintain the temperature above 50 °C for several minutes to achieve complete tumor cell death; however, such high temperatures may damage the surrounding normal tissues. Mild PTT (<45 °C) is key in achieving effective treatment while preventing damage to normal tissues caused by hyperthermia. Recently, mild PTT has been achieved by combining this type of therapy with other treatment modalities or by weakening the heat resistance of tumor cells [20,21]. The development of NIR-II GNB-based strategies that effectively destroy tumors under mild-temperature heating is important for the clinical translation of future therapeutic approaches for NSCLC.

Bioinformatics is a powerful tool for screening and designing nanomedicines with potential therapeutic effects. In particular, network pharmacology serves as an emerging bioinformatics analysis tool that can reveal the therapeutic application and mechanism of traditional Chinese medicine (TCM) by constructing drug-target-pathway network models [22]. Recently, many researchers have utilized network pharmacology to design nano-TCMs and predict their therapeutic effects and mechanisms of action in vivo. For example, Qin et al. employed network pharmacology analysis to reveal that inhibition of the inflammatory response is the mechanism of action of berberin for treating myocardial infarction. On the basis of these results, they prepared platelet membrane-coated berberin nanoparticles, which were used to decrease the amount of inflammation-related macrophages and apoptotic cardiomyocytes in the infarcted rat myocardium [23]. Moreover, Liu et al. employed network pharmacology to predict and investigate the mechanism of action of arctiin in the treatment of osteoarthritis and developed a long-acting hydrogel platform loaded with arctiin for the sustained treatment of osteoarthritis [24]. Therefore, it is possible to screen natural drugs that act on HSP90 and design nano-TCMs suitable for enhanced mild PTT via bioinformatic analysis.

In this study, we first screened natural drugs that act on HSP90 using bioinformatics and finally selected curcumin (Cur) to load in NIR-II-responsive GNBs to induce mild PTT based on molecular docking results. Subsequently, we conducted an evaluation of the potential efficacy and underlying mechanisms of Cur in the treatment of NSCLC through application of network pharmacology. As shown in Scheme 1, NIR-II responsive GNBs loaded with Cur (GNBs-Cur) were strategically designed and prepared via hydrophobic-hydrophobic interactions and hydrogen bonds [25–29]. After tail vein administration, GNBs-Cur could enrich the tumor area through their long circulation time and EPR effects. When the tumor was exposed to NIR-II laser, the temperature of the tumor increased rapidly to 43 °C, whereas Cur loaded on the GNBs was quickly released. Subsequently, the released Cur not only downregulates the overexpressed HSP90 to decrease the thermoresistance of tumor cells but also blocks the PI3K/AKT pathway to suppress the anti-apoptotic signal caspase 3. Ultimately, enhanced mild PTT combined with low-dose Cur-mediated chemotherapy demonstrated excellent antitumor effects both in vitro and in vivo. In conclusion, the as-prepared NIR-II responsive GNBs-Cur nanoplatforms provide new insights into achieving synergistic mild PTT and chemotherapy, which demonstrates tremendous potential for effective treatment of NSCLC.

2. Materials and methods

2.1. Materials

Curcumin (Cur) was obtained from Macklin Biochemical Co., Ltd., China; gold (III) chloride hydrate ($HAuCl_4{\cdot}3H_2O$), cetyltrimethylammonium bromide (CTAB), cetyltrimethylammonium chloride (CTAC), silver nitrate ($AgNO_3$), L-ascorbic acid (AA), and 4′,6-Diamidino-2-phenylindole (DAPI) were obtained from Aladdin Reagent Co., Ltd., China; hydrochloric acid (HCl), nitric acid (HNO_3), sodium borohydride ($NaBH_4$), and sodium hydroxide (NaOH) were purchased from Sinopharm Chemical Reagent Co. Ltd., China; fetal bovine serum (FBS) was purchased from Gibco Life Technologies, USA; Ham's F-12K culture medium was obtained from Wuhan Servicebio Technology Co., Ltd, China; phosphate buffer saline (PBS) powder, dimethylsulfoxide (DMSO), and a Calcein-AM/PI Double Stain Kit were purchased from Beijing Solarbio Science & Technology Co., Ltd., China; Cy5.5 was provided by Xi'an ruixi Biological Technology Co., Ltd., China; cell counting kit-8 (CCK-8) was purchased from ZETA life, USA; an Annexin V-FITC/PI Apoptosis Detection Kit was purchased from Jiangsu Keygen Biotexh Corp., Ltd, China; antibodies against HSP90 and anti-AKT were obtained from Wuhan Servicebio Technology Co., Ltd, China; anti-p-Akt antibody was sourced from Cell Signaling Technology, USA; and antibodies against p-PI3K and PI3K were purchased from Abcam, UK.

2.2. Drug discovery for targeting HSP90

Potential molecular compounds targeting HSP90 were identified using the HIT2.0 database and the Therapeutic Target Database (TTD). HIT2.0 (http://hit2.badd-cao.net) was designed to provide information about herbal ingredients and target foods [30]. The TTD (https://idrblab.org/ttd/) is a database that offers information about therapeutic proteins and their corresponding drugs/ligands [31]. We evaluated the drug-likeness and biological activities of the compounds using Swiss ADME (http://www.swissadme.ch/) [32], and compounds with a bioavailability score greater than 0.65 and passing drug similarity filters (Lipinski, Ghose, Veber, Egan and Muegge) were further screened.

Molecular docking is a simulation method that predicts the conformation of drug molecules in the appropriate target binding site and evaluates their binding affinity. The structures of the compounds were obtained from the PubChem database, and the structure of HSP90 was determined through the protein database (PDB, http://www.rcsb.org/). We processed the ligands and receptors using AutoDock Tools with default options and performed docking calculations using AutoDock Vina with default parameters [33]. In molecular docking, more negative affinity scores for the docking pose indicate stronger binding affinity. The docking results were visualized using Discovery Studio.

2.3. Bioinformatic analysis of the effect of Cur on NSCLC

The targets of Cur were obtained from the symMap (http://www.symmap.org/), TCMSP (https://old.tcmsp-e.com/tcmsp.php), and Swiss Target Prediction (http://www.swisstargetprediction.ch/) databases [34–36]. Based on the genetic information from the Uniport database, all curcumin target proteins were uniformly mapped to gene names for subsequent analyses. In addition, the DisGeNet and GeneCards databases were used to identify disease genes associated with lung cancer. After de-duplication of the genes obtained from these databases, a Venn diagram was utilized to visualize the intersection between Cur target genes and lung-related genes. Using the STRING (https://string-db.org) database [37], the interaction genes between Cur and NSCLC were considered as the core genes, and then were analyzed to generate a protein–protein interaction (PPI) network, with the confidence score set to 0.4. The PPI data were submitted to Cytoscape, and the molecular complex detection algorithm (MCODE) plugin was utilized to identify the hub gene with the following parameters: K-Core = 2, degree cutoff = 2, and node score cutoff = 0.2 [38]. Based on the Metascape (https://metascape.org/) database, Gene Ontology (GO) annotation and Kyoto Encyclopedia of Genes and Genomes (KEGG) analyses was conducted to explore the biological functions and molecular mechanisms of target genes [39]. Min overlap = 2, Min Enrichment = 1.5, and $P < 0.01$ were selected as advanced options. To preliminarily verify the key role of the screened hub target gene in lung cancer, we collected the GSE75037 expression profile data from the Gene Expression Omnibus (GEO) (https://www.ncbi.nlm.nih.gov/geo/) database for differential expression analysis. GSE75037 is an expression profile of 83 matched pairs of lung adenocarcinomas and non-malignant adjacent tissues. The "Limma" package was used to perform differential expression analysis of the target gene between the normal and tumor groups [40]. Kaplan–Meier curves, derived from the Gene Expression Profiling Interactive Analysis (GEPIA) (http://gepia.cancer-pku.cn/) database, were employed to investigate the association between core gene expression levels and the overall survival rate of patients diagnosed with lung cancer [41].

Molecular docking is a simulation method that predicts the conformation of small drug molecules in the appropriate target binding site and evaluates their binding affinity. The structure of Cur was determined through the PubChem database, and the structure of the hub target protein was acquired from the protein database (PDB, http://www.rcsb.org/). We processed the ligands and receptors using AutoDock Tools with default options and performed docking calculations using AutoDock Vina with default parameters [33]. The docking results were visualized using Discovery Studio.

2.4. Synthesis of GNBs@PEG-COOH

To synthesize GNBs@PEG-COOH, 10 mL of $HAuCl_4$ (0.25 mM) was added to CTAC solution (50 mM), and 0.25 mL of freshly prepared $NaBH_4$ (25 mM) was mixed with the above mixture, before vigorous stirring at 37 °C. Gold seeds were formed when the color of the solution changed from pale yellow to brown. The mixture was subsequently reacted at 80 °C and stirred for 90 min in an oil bath until the color of the solution gradually changed from brown to red. Finally, the heat-treated seed solution was separated from the bath and kept at 37 °C. The final concentration of Au was 0.25 mM.

An aqueous solution containing 100 mL of CTAB (100 mM), 5 mL of $HAuCl_4$ (10 mM), 1 mL of $AgNO_3$ (10 mM), 2 mL of HCl (2 M), and 0.8 mL of AA (100 mM) was added to 5 mL of seed solution (0.25 mM). This mixture was then stirred and subsequently reacted at 80 °C for 90 min. Finally, the ultimate GNB products were centrifuged and washed three times using deionized water. Subsequently, SH-PEG_{5K}-COOH was employed to modify the surface of GNBs. The PEG-modified GNBs were prepared by introducing SH-PEG_{5K}-COOH into the GNBs solution, followed by stirring with a magnetic stirrer for 24 h. The resulting solution was then subjected to ultrafiltration using a 100 kDa ultrafiltration tube at 4000 rpm for 15 min. The precipitate was collected and washed three times with purified water to ensure purity.

2.5. Synthesis of GNBs-Cur and GNBs-Cur-Cy5.5

Approximately 1 mM of Cur was dissolved in DMSO solution. Subsequently, 100 μL of Cur DMSO solution was added to 2 mL of GNBs@PEG-COOH (200 μg/mL) solution and stirred gently for 12 h. The precipitate was isolated by centrifuging at 3000 rpm for 10 min. The precipitate was washed several times using ultrapure water to obtain GNBs-Cur, which was dispersed in 2 mL of ultra-pure water under ultrasound. Furthermore, GNBs-Cur and Cy5.5 were combined and gently agitated for 12 h at 37 °C. Subsequently, the resultant mixture was placed into a dialysis bag and subjected to dialysis for an additional 12 h to eliminate unbound Cy5.5. The precipitate was then isolated by centrifugation at 3000 rpm for 10 min, followed by multiple washes with ultrapure water to yield GNBs-Cur-Cy5.5.

2.6. Characterization

TEM and SEM imaging was conducted using an HT7700 (Hitachi, Japan) and an S-4800 (Hitachi, Japan), respectively. Both the size profile and zeta potential were investigated via dynamic light scattering (DLS) using a nanoparticle analyzer (SZ-100V2, Horiba, Japan). The ultraviolet–visible (UV–vis) absorption and fluorescence (FL) spectra were recorded using a UV–vis spectrophotometer (UH5700, HITACHI, Japan) and an FL spectrophotometer (F-7000, Hitachi, Japan), respectively. For in vitro PA imaging, solutions containing different concentrations of GNBs-Cur (12.5, 25, 50, 100 and 200 μg/mL) were placed in tubes, and the PA signal was detected.

The Cur release profile was examined in PBS at pH values of 7.4 and 5.5. GNBs-Cur was encapsulated in a dialysis bag with a molecular weight cut-off (MWCO) of 3.0 kDa, which was subsequently immersed in 30 mL PBS and subjected to gentle agitation at 37 °C. At designated intervals, 3 mL of the release medium was withdrawn and replaced with an equivalent volume of fresh medium. Additionally, at various time points, the dialysis bag in PBS (pH 5.5 and 7.4) was exposed to irradiation with a 1064 nm laser (1.0 W/cm^2, 5 min) [42]. The cumulative release of Cur was quantitatively assessed using UV–visible absorption spectroscopy.

2.7. Photothermal performance

To investigate the photothermal capability, the GNB stock solution was diluted into a series of solutions of 50, 100 and 200 μg/mL. Next, 100 μL of the GNB solution at distinct concentrations was exposed to a 1064 nm laser (1.0 W/cm^2, 5 min), and the temperature variations were monitored using a handheld thermal imaging camera at intervals of 30 s. Alternatively, by varying the power density (0.5, 1.0, and 2.0 W/cm^2), the temperature of the GNBs (100 μg/mL) was monitored for 5 min of light irradiation. Furthermore, the photothermal stability of GNBs was investigated through laser on/off cycle experiments. Next, 100 μL of GNBs (100 μg/mL) was irradiated for 5 min and then naturally cooled for 4 min, and the procedure was performed for four cycles. The temperature profile of the GNBs was also recorded utilizing a handheld thermal imaging camera (HM-TPK20-3AQF/W, Hikmicro, China).

The photothermal conversion efficiency (η) was calculated using the following equation:

$$\eta = \frac{hS\left(T_{max} - T_{max,H_2O}\right)}{I\left(1 - 10^{-A_\lambda}\right)} \tag{1}$$

$$hS = \frac{mC_p}{\tau_s} \tag{2}$$

$$\tau = -\frac{t}{Ln\left(\frac{T - T_{surr.}}{T - T_{max}}\right)} \tag{3}$$

In Equation (1), h is the heat transfer, S is the container's surface area, T_{max} and $T_{max,H2O}$ are the maximum equilibrium temperatures of the sample (GNBs-Cur) and water, respectively, I is the incident laser powder, and A_λ is the absorbance of GNBs-Cur at 1064 nm. In Equation (2), m and Cp represent the mass of the sample and heat capacity of water (J/g·°C), respectively, and τ_s is the time constant for heat transfer calculated using Equation (3). In Equation (3), t and Tsurr denote the time and ambient temperature of the surroundings, respectively. According to the above equation, the photothermal conversion rate of GNBs-Cur was approximately 37.7 % under irradiation by a 1064 nm laser.

2.8. Cell culture

The A549 lung cancer cells were acquired from the BeNa Culture Collection (China). A549 lung cancer cells were cultured in F-12K culture medium containing 10 % FBS, 1 % penicillin, and 1 % streptomycin.

2.9. Cellular uptake

A549 cells were inoculated in a well of chambered coverglass (5 × 10^4 cells per well) and cultured for 12 h. Then, solutions of free Cur or GNBs-Cur were replaced with the cell growth media, and cells were incubated for the designed time (1, 2, and 4 h). Subsequently, A549 cells were washed using PBS and then fixed with 4 % paraformaldehyde solution. The nuclei of cells were stained with DAPI and then observed through a confocal laser scanning microscope (CLSM, TCS SP8, Leica, Germany).

For flow cytometry (FC) analysis, A549 cells were inoculated in 24-well plates (2 × 10^5 per well) and cultivated for 12 h. Subsequently, cells were treated with free Cur or GNBs-Cur for the designed time (1, 2, and 4 h). Finally, the cells were collected to analyze the cellular endocytosis of GNBs-Cur using FC (FACSCanto II, BD Biosciences, USA).

2.10. In vitro therapeutic efficacy

Cytotoxicity was determined using CCK-8 assays. A549 cells were cultured in 96-well plates (1 × 10^5 per well) and incubated for 12 h. Subsequently, 100 μL fresh medium containing GNBs, Cur, or GNBs-Cur was replaced with the original culture medium (GNB dose: 0–200 μg/mL, Cur dose: 0–20 μM). After 4 h of incubation, cells were washed several times using PBS and subsequently treated with or without light irradiation for 5 min (1064 nm, 1 W/cm^2). After 16 h of further incubation, cell viability was analyzed using a Multiskan FC microplate reader (BioTek, USA). Moreover, living and dead cells were stained using a Calcein-AM/PI double staining kit after different treatments. The results of cell imaging were obtained using a FL microscope (EVOS, Thermo Scientific, USA).

A549 cells were placed in 24-well plates (1 × 10^6 per well) and incubated for 12 h. Then, original F12-K was replaced with the same amount of fresh medium containing Cur, GNBs, or GNBs-Cur with an equal Cur concentration (20 μM) and GNB concentration (100 μg/mL). After incubation for 4 h, the NIR, GNBs + NIR, and GNBs-Cur + NIR groups were irradiated with laser (1 W/cm^2, 5 min). After an extra 20 h of incubation, cells were washed with PBS and digested with EDTA-free trypsin. Cells were collected and stained using the Apoptosis Detection Kit, and the apoptosis rate of cells was detected using the FC.

2.11. Western blotting

The method of cell treatments was similar to that used for apoptotic analysis. Subsequently, cells were collected and lysed using a RIPA lysis buffer, and the supernatant containing cell total proteins was obtained via centrifugation (12000 rpm). Cell proteins were separated by SDS-PAGE and transferred to PVDF membranes. Subsequently, the membranes were submerged in 5 % nonfat milk for 1 h to facilitate blocking, followed by incubation with primary antibody overnight and further incubation with secondary antibody for 0.5 h at 37 °C. A chemiluminescence system (ChemiScope 6000, Clinx, China) was utilized to visualize the target protein bands.

2.12. Establishment of the tumor model

BALB/c female nude mice were obtained from Zhuhai BesTest Bio-Tech Co., Ltd. (China). A549 tumor-bearing mice were established via subcutaneous injection of A549 cells (5 × 10^6) into the right flank of each mouse. Mice were treated for subsequent in vivo experiments until the average tumor volume reached about 80 mm^3. All experiments were carried out at the Experimental Animal Center of Guangdong Medical University and were approved by the Animal Welfare and Ethical Committee of Guangdong Medical University (Permit No. SYXK 2019-

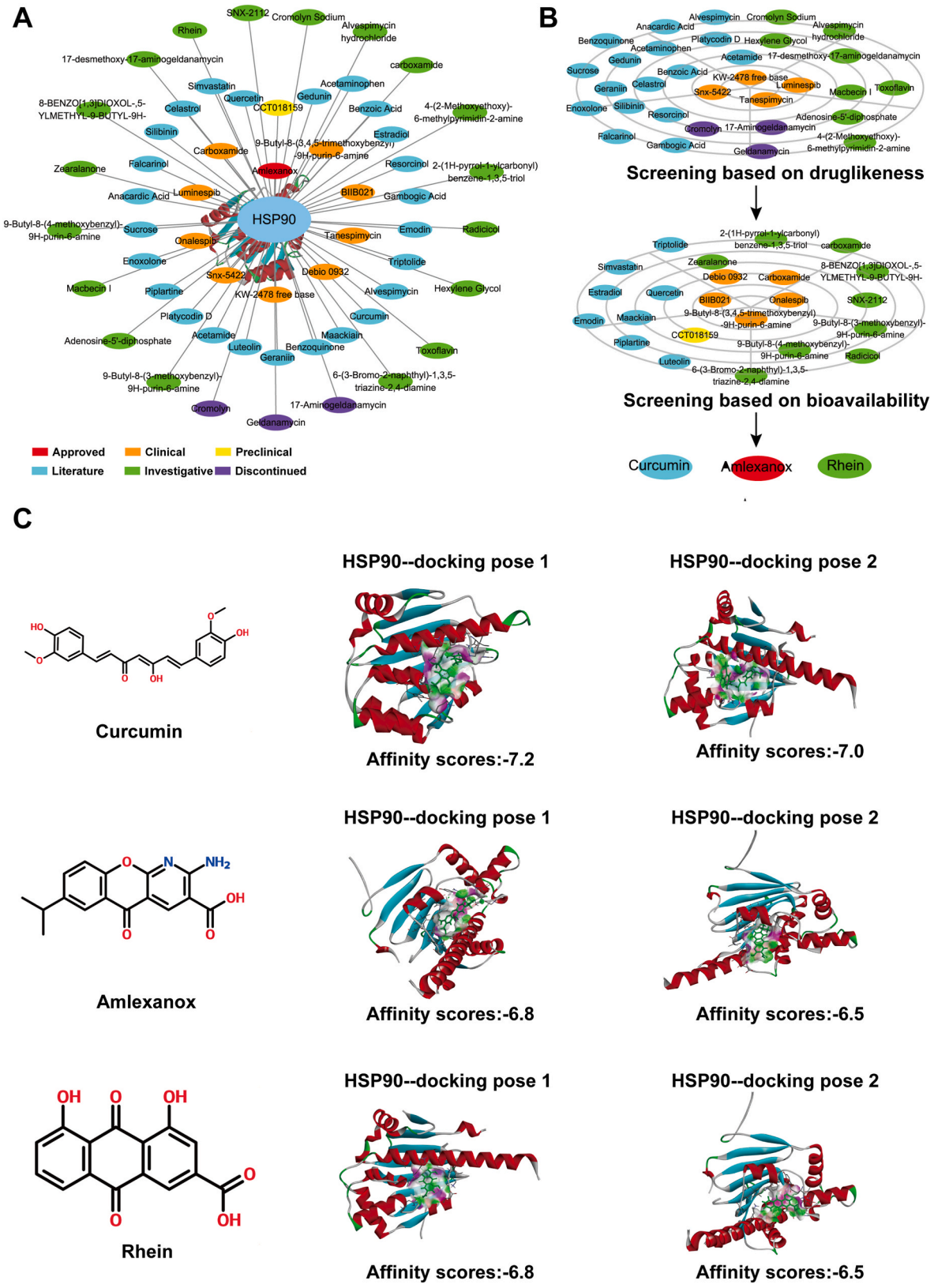

Fig. 1. Landscape of the HSP90 target compound screening. **(A)** Network of compounds targeting HSP90. Different colored nodes represent the research status of the drug. **(B)** Drug screening patterns based on drug-likeness and bioavailability. **(C)** Molecular docking simulations of three target compounds (curcumin, amlexanox, and rhein) with HSP90.

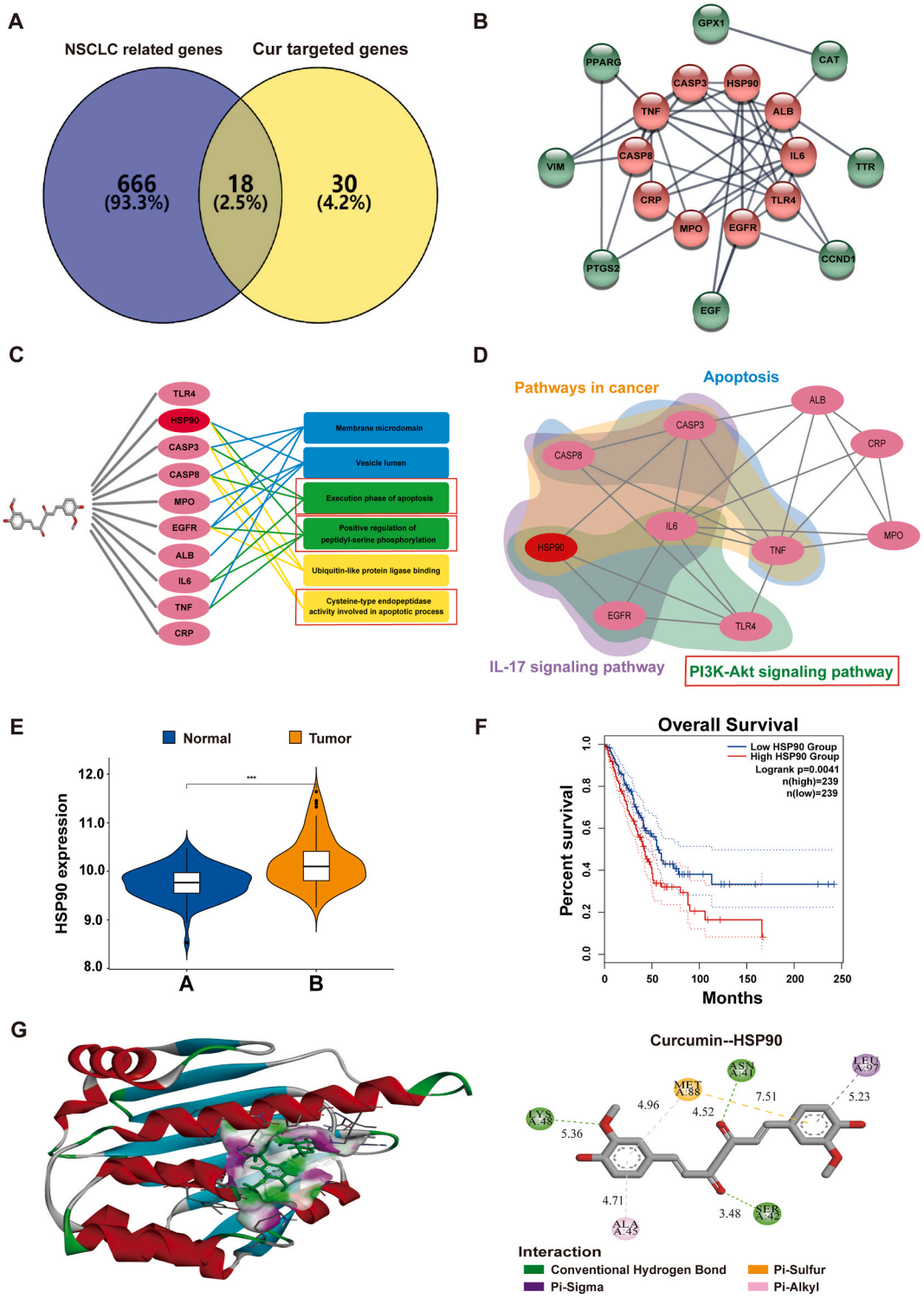

Fig. 2. Bioinformatics analysis of Cur in NSCLC. **(A)** Venn diagram of common genes between Cur and NSCLC. **(B)** Nodes represent proteins, and red nodes represent hub targets. The connection lines between nodes represent interactions between proteins. **(C)** Cur–target–GO network. The blue box is the Gene Ontology (GO) term of cell component; the green box is the GO term of biological processes; and the yellow box is the GO term of molecular function. **(D)** Gene-pathway network. The genes in the same color palette demonstrate that they are enriched in the same pathway. **(E)** Transcriptome expression levels of the key target HSP90 in normal and NSCLC samples. **(F)** Correlation between HSP90 expression and NSCLC prognosis. **(G)** Molecular docking simulation of Cur binding to HSP90 protein. The circular nodes represent the amino acid residues that interact with Cur. (For interpretation of the references to color in this figure legend, the reader is referred to the Web version of this article.)

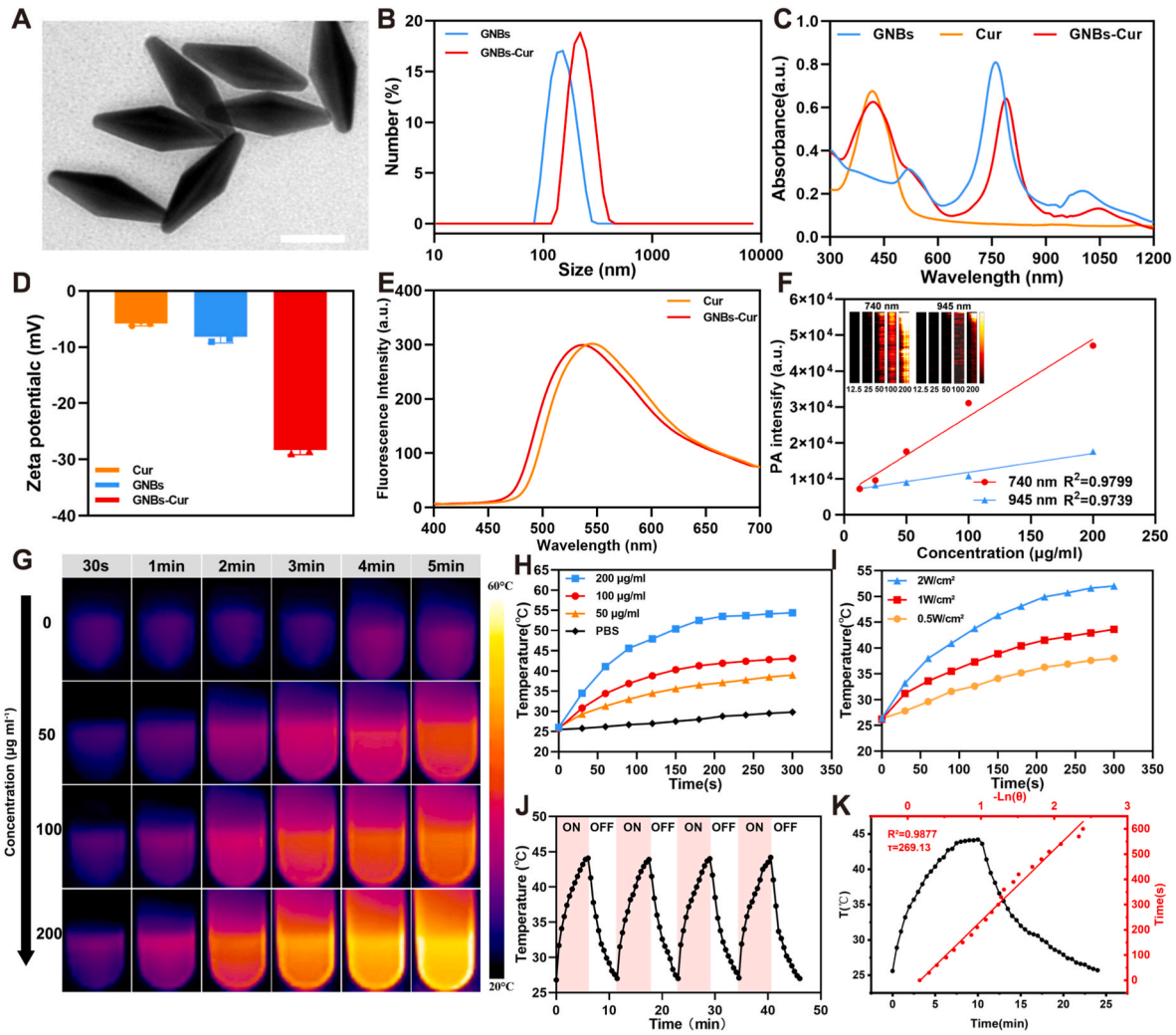

Fig. 3. Characterization and photothermal study of GNBs-Cur. **(A)** TEM image of GNBs-Cur (scale bar = 50 nm). **(B)** Size distribution curves of GNBs and GNBs-Cur. **(C)** UV–vis spectra of Cur, GNBs, and GNBs-Cur. **(D)** Zeta potential analysis of Cur, GNBs, and GNBs-Cur. **(E)** Fluorescence spectra of Cur and GNBs-Cur. **(F)** PA intensity of GNBs-Cur at distinct concentrations under 740 nm and 945 nm laser excitation. **(G)** Thermal images of GNBs-Cur at various concentrations under NIR-II laser irradiation (1 W cm^{-2}) and **(H)** corresponding photothermal curves. **(I)** Temperature changes of GNBs-Cur upon laser irradiation at different intensities. **(J)** Temperature evolution of GNBs-Cur after four heating−cooling cycles. **(K)** Temperature profiles of GNBs-Cur upon laser irradiation and upon no laser irradiation.

0213).

2.13. In vivo photoacoustic/fluorescence imaging

Mice were intravenously injected with GNBs-Cur (2 mg/kg GNBs) for PA imaging. The PA signal at the tumor region was captured at designated time points (2, 4, 8, 12, and 24 h) via the Vevo LAZR-X imaging system (λ_{ex} = 740 nm and λ_{ex} = 945 nm). For FL imaging, Cy5.5 was selected as the fluorescent probe, and GNBs-Cur loaded with Cy5.5 (GNBs-Cur-Cy5.5) was developed. After intravenous injection of GNBs-Cur-Cy5.5, FL images of mice were obtained at distinct time points (2, 4, 8, 12, and 24 h) through an IVIV Lumina II optical imaging system (Caliper, USA). FL signals from major organs and tumors were monitored for ex vivo imaging.

2.14. Mild photothermal-chemo synergistic therapy

A549 tumor-bearing nude mice were randomly separated into five groups (n = 5 per group): PBS, GNBs + NIR, Cur, GNBs-Cur, and GNBs-Cur + NIR. Mice were intravenously injected with PBS, Cur, GNBs, or GNBs-Cur (GNBs: 2 mg/kg, Cur: 50 mg/kg). For the GNBs + NIR and GNBs-Cur + NIR tumors, the tumors were exposed to a laser (1064 nm, 1 W/cm^{-2}, 6 min) 4 h post-injection. A thermal imaging camera was employed to continuously monitor the temperature changes at the tumor sites in real time. During the 16 days, tumor sizes and body weights of mice were recorded every 2 days. Mice were sacrificed, and their tumors were anatomized at the last moment. The isolated tumors were stained with hematoxylin and eosin (H&E) to assess the antitumor effect. Immunofluorescent staining with TUNEL, Ki-67, HSP90, and caspase 3 in tumors was further performed to evaluate the therapeutic efficacy in vivo.

2.15. In vivo safety evaluation

After 16 days of treatment, the mice were euthanized and their blood was collected to determine the clinical biochemical indices. Major organs were harvested for histological analysis via H&E staining.

A549 tumor-bearing nude mice were randomly selected and intravenously injected with GNBs-Cur. After post-injection for 4 h, mice were irradiated with laser at an intensity of either 1 W/cm^2 (43 °C) or 1.5 W/cm^2 for 6 min (58 °C). Histological analysis was conducted using H&E staining of tumors and the surrounding skin tissue.

2.16. Statistical analysis

The significance of differences between two comparative groups was assessed through one-way analysis of variance, and the distinctions between multiple groups were evaluated by the Student's *t*-test (ANOVA).

3. Results and discussion

3.1. Drug discovery for targeting HSP90

In this study, 57 potential molecular compounds targeting HSP90 were identified from the HIT2.0 and TTD databases (Fig. 1A). Based on the drug-likeness parameters and bioavailability score of each compound provided by the Swiss ADME database (Table S1), we finally screened three small-molecule compounds, namely Cur, amlexanox, and rhein (Fig. 1B). To further evaluate the targeting ability of these compounds to HSP90, molecular docking was used to analyze their docking pose and binding strength. Among the three compounds, Cur exhibited the strongest binding pose (affinity score = −7.2) to HSP90 and was identified as a promising compound targeting HSP90 (Fig. 1C).

3.2. Prediction of the molecular mechanism of Cur in NSCLC

After gene name standardization, 48 Cur-targeted genes were predicted from the symMap, TCMSP, and Swiss Target Prediction databases, whereas 684 genes were retrieved from a combination of the DisGeNET and GeneCards databases for NSCLC. Venn diagrams showed that 18 genes were associated with both Cur and NSCLC (Fig. 2A). To explore the potential inter-protein interactions among these 18 genes, a PPI network was developed via the STRING database. Analysis of the complex regulatory network revealed that these genes cross-talk with each other, and 11 hub genes were crucial nodes of the whole network (Fig. 2B). GO enrichment was conducted to better elucidate the biological characteristics of the 11 hub genes of Cur in NSCLC at a systematic level. Fig. 2C shows the Cur–target–GO terms network, in which the hub genes were mapped to the vesicle lumen (ALB/EGFR/HSP90/MPO), membrane microdomain (CASP3/CASP8/EGFR/TNF), execution phase of apoptosis (CASP3/CASP8/IL6), regulation of protein serine/threonine kinase activity (EGFR/HSP90/IL6/TNF), cysteine-type endopeptidase activity involved in the apoptotic process (CASP3/CASP8), and ubiquitin-like protein ligase binding (CASP8/EGFR/HSP90). KEGG enrichment analysis indicated that the effects of Cur on the inhibition of NSCLC were related to the pathways, including pathways in cancer, apoptosis, IL-17 signaling, and PI3K-Akt signaling (Fig. 2D). It is generally recognized that PI3K-Akt signaling is correlated with the proliferation, migration, and anti-apoptosis of tumor cells involving HSP90 [43]. Therefore, these data provide preliminary theoretical evidence for HSP90 as a key target of Cur for treating NSCLC. Further differential expression analysis suggested that HSP90 expression was significantly higher in the tumor group than in the normal group (Fig. 2E). Additionally, patients in the low-HSP90 group had better overall survival (OS) than those in the high-HSP90 group (Fig. 2F). Molecular docking revealed that the Cur and surface deep cavity of HSP90 exhibited good shape complementarity and a superior binding mode (Fig. 2G). The residues that interacted with the ligand included Ala 45, Asn 41, Leu 79, and Met 88. In addition, individual amino acid residues, such as Asn41, Lys48, and Ser42, can form hydrogen bonds with the oxygen atoms of the ligand, which contributes to their interaction and close bonding.

3.3. Preparation and characterization of GNBs-Cur

The primary synthesis procedure for GNBs-Cur nanoparticles is depicted in Scheme 1. GNBs were prepared using the seeded growth method [44]. Morphological characterization results obtained using TEM and SEM indicated that PEG modified GNBs and GNBs-Cur both exhibited biconical structures and were evenly dispersed (Fig. 3A–S1 and S2). The transverse and longitudinal sizes of the GNBs were approximately 38 and 136 nm, respectively. The optimized loading rate of Cur was approximately 42.2 % ± 3.5 %, indicating the high loading efficiency of GNBs (Fig. S3). Due to the efficient attachment of Cur to the surface of GNBs, the hydrodynamic size of GNBs-Cur (218.6 ± 14 nm) was fractionally larger than that of GNBs (151.57 ± 10 nm), as indicated by DLS measurements (Fig. 3B). As illustrated in Fig. 3C, GNBs exhibit characteristic absorption peaks at wavelengths of 1020 nm, 760 nm, and 530 nm, while Cur displayed a distinct absorption peak at 425 nm. The secondary peak at 1020 nm likely results from metal atom substitution during synthesis, altering the surface atomic arrangement and creating a new plasmon resonance peak. The composite GNBs-Cur demonstrated absorption peaks at 1040 nm, 780 nm, and 425 nm, indicating a red shift of approximately 20 nm attributable to the incorporation of Cur. Additionally, Cy5.5 was characterized by an absorption peak at 680 nm, and the GNBs-Cur-Cy5.5 complex exhibited a peak at 690 nm, reflecting the influence of Cy5.5 loading (Fig. S4). Fig. 3D shows that the zeta potentials of Cur, GNBs, and GNBs-Cur were −5.79 ± 0.43 mV, −8.17 ± 1.06 mV, and −28.33 ± 0.81 mV, respectively. The zeta potential of the nanoparticles significantly changed from −8.17 ± 1.06 mV (GNBs) to −23.80 ± 0.62 mV (GNBs-Cur) when negatively charged Cur joined the GNBs. These results imply that the Cur was successfully loaded on the GNBs. The release profile of Cur from GNBs-Cur was evaluated utilizing the dialysis bag diffusion method. Under acidic conditions combined with laser irradiation, the release of Cur from GNBs-Cur achieved approximately 60 % within a 24 h period (Fig. S6). Additionally, the FL/PA performances of GNBs-Cur were investigated by spectral analysis. The FL spectra of Cur and GNBs-Cur exhibited similar FL curves, suggesting that the fluorescent performance of Cur remained unchanged after loading of Cur (Fig. 3E). The fluorescence emission spectra of both free Cy5.5 and GNBs-Cur-Cy5.5 demonstrated a peak emission at approximately 690 nm, thereby confirming the successful incorporation of Cy5.5 (Fig. S5). In addition, the PA intensities of GNBs-Cur at 740 and 945 nm gradually increased with increasing concentration of GNBs-Cur (Fig. 3F). When the concentration was increased from 12.5 μg/mL to 200 μg/mL, the PA signal of GNBs-Cur improved and resulted in brighter images. The PA signal exhibited a linear correlation with the concentration of GNBs-Cur, demonstrating the robust in vitro PA imaging capability of GNBs-Cur. These findings suggest that GNBs-Cur can be successfully created with excellent biocompatibility and excellent FL/PA imaging performance for biological applications.

3.4. PTT analysis of GNBs-Cur in vitro

GNBs exhibit high photothermal conversion efficiency in PTT because of their relatively bright surface plasmon resonance (SPR) absorption bands in the NIR region [45]. In this experiment, the photothermal conversion properties of GNBs under NIR-II irradiation were investigated. The impact of the photothermal effect of GNBs-Cur solutions at various concentrations was first explored. As illustrated in Fig. 3G and H, the temperature of GNBs-Cur solutions increased progressively upon irradiation with a 1064 nm laser for 5 min as the concentration of GNBs increased from 0 to 200 μg/mL. At a GNB concentration of 100 μg/mL, the temperature changed from 25.7 °C to 43.1 °C and stabilized after 5 min of irradiation, indicating mild PTT. The correlation between laser power densities and temperature variations was further investigated. The temperature of GNBs-Cur solutions reached 38.0 °C, 43.6 °C, and 52.0 °C when irradiated at power densities of 0.5, 1.0, and 2.0 W/cm^2, respectively (Fig. 3I). The photothermal stability of GNBs-Cur was then confirmed by the negligible attenuation of the recorded temperatures from four times "on/off" cycles of laser irradiation (Fig. 3J). By measuring the temperature changes during the heating and cooling phases, the time constants (τs) of the thermal cooling process were calculated to be 269.13 s, and the corresponding

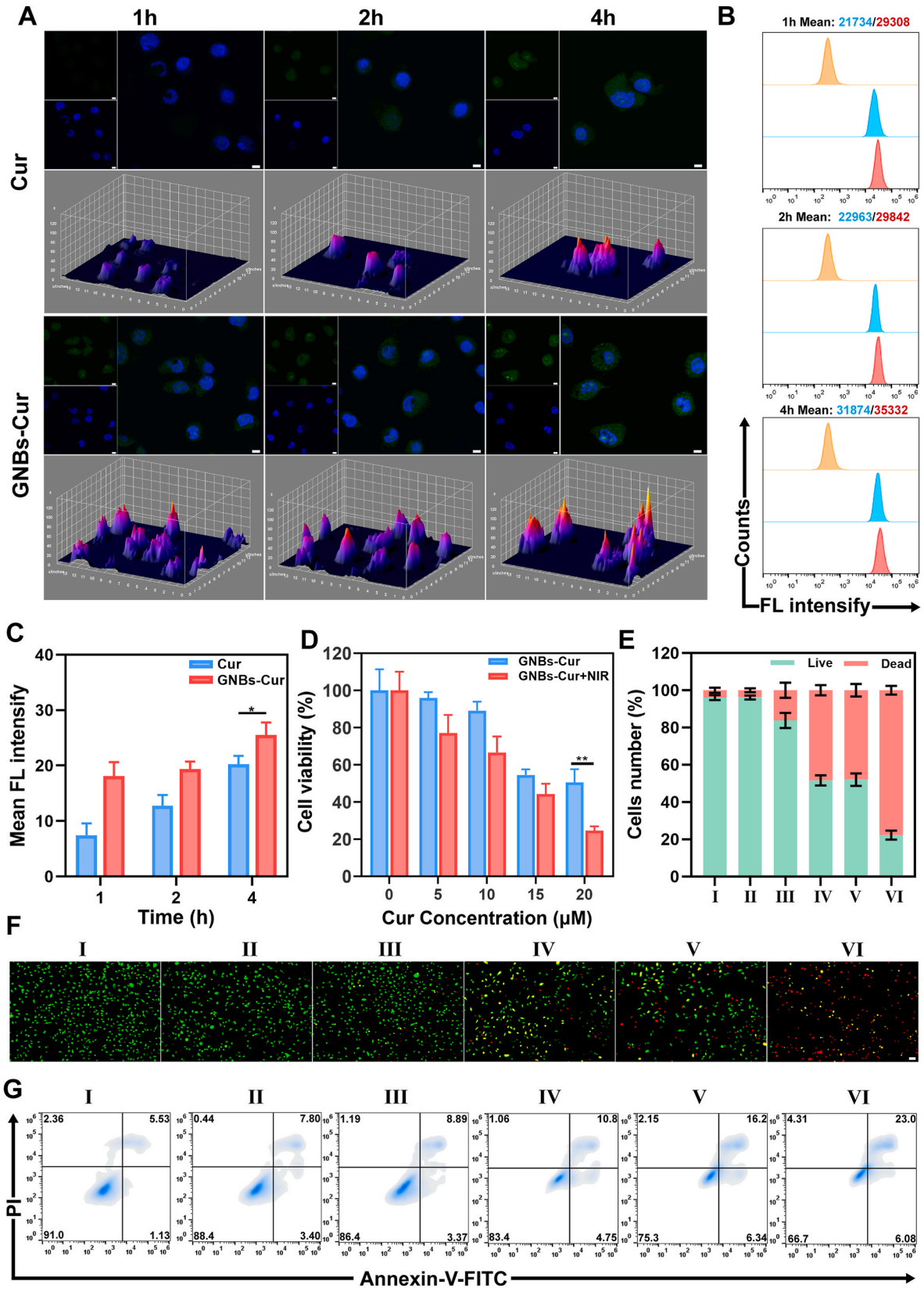

Fig. 4. In vitro evaluation of the therapeutic effect of GNBs-Cur. **(A)** Representative confocal laser scanning microscope (CLSM) images of A549 cells treated with free Cur and GNBs-Cur at different time points (scale bar = 5 μm). **(B)** Flow cytometry analysis of A549 cells interacted with free Cur and GNBs-Cur at various time points. **(C)** Semiquantitative fluorescence intensity of A549 cells incubated with free Cur and GNBs-Cur at different time points. **(D)** CCK-8 method for the survival rate of A549 cells treated by GNBs-Cur with and without laser irradiation. **(E)** Quantification of the percentage of viable and dead cells in (F). **(F)** Live/dead staining study of A549 cells after distinct treatments (scale bar = 50 μm). **(G)** Apoptosis analysis of A549 cell after different treatments. I) PBS, II) NIR, III) GNBs + NIR, IV) Cur, V) GNBs-Cur, and VI) GNBs-Cur + NIR. Data are presented as the mean ± S.D (n = 3). *p < 0.05, **p < 0.01.

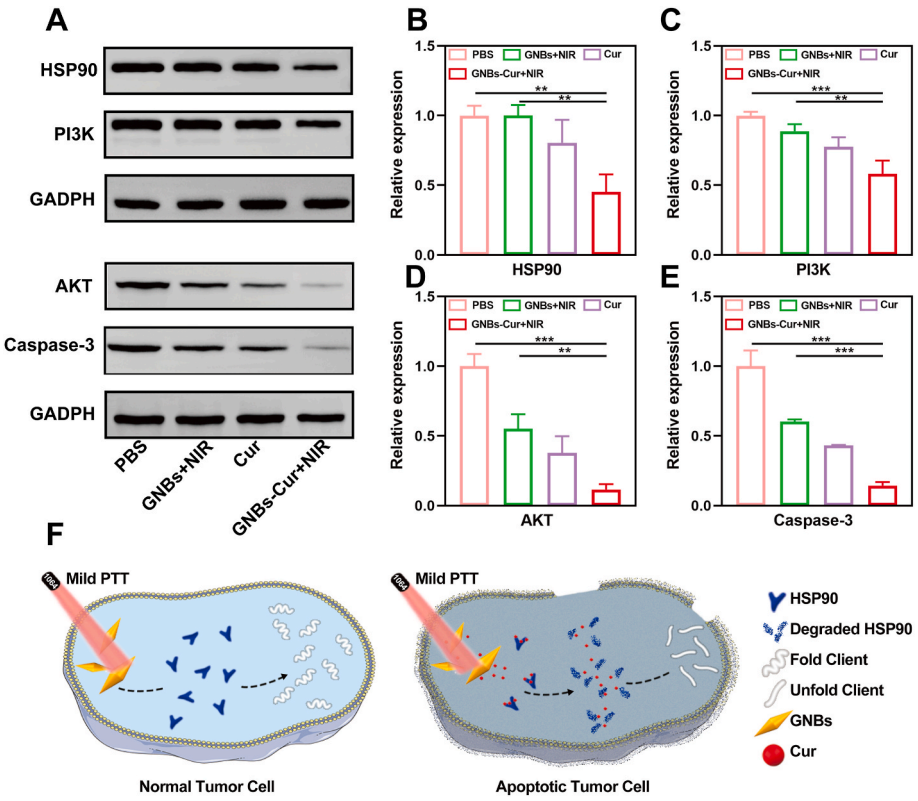

Fig. 5. In vitro mechanisms of enhanced mild PTT and chemotherapy. (A) Western blot analysis of HSP90, PI3K, AKT, and caspase 3 expression in A549 cells after various treatments. (B–E) Quantification of HSP90, PI3K, AKT, and caspase 3 levels. Data are shown as the mean ± S.D (n = 3). *p < 0.05, **p < 0.01, ***p < 0.001. (F) Schematic illustration of GNBs-Cur optimized synergistic mild PTT and chemotherapy.

photothermal conversion efficiency was 37.7 % (Fig. 3K). Finally, we confirm that Cur loading does not affect the photothermal properties of GNBs, with no remarkable change in the temperature of the PBS and Cur solutions (Fig. S7). However, discernible heat elevation was observed in the GNBs and GNBs-Cur solutions, which exhibited similar photothermal effects (≈43 °C). These results indicate that GNBs-Cur exhibits favorable heat generation under laser irradiation and has great potential as a photothermal agent for mild PTT.

3.5. Cellular uptake and proapoptotic effects in vitro

The internalization process of GNBs-Cur was investigated using a CLSM and a flow cytometer. As illustrated in Fig. 4A, cells were incubated with free Cur or GNBs-Cur, and the FL signal was observed at different times (1, 2, and 4 h). After the first 1 h, both groups showed dot FL with weak green signals, implying that Cur and GNBs-Cur nanoparticles were initially ingested by A549 cells. The intensity of the intracellular green FL signal gradually increased over time, indicating that tumor cells took up more drugs. After 4 h of endocytosis, the FL intensity was significantly increased compared to that after 1 h. Notably, the green signal of the GNBs-Cur group was brighter than that of the free Cur group, suggesting that the GNBs play a role in facilitating Cur entry into the cells because of their good biocompatibility and delivery capacity. Next, quantitative analysis of cellular uptake was performed by flow cytometry (Fig. 4B). The result also showed that cellular uptake behavior was time-dependent, and after 4 h of endocytosis, the FL intensities of free Cur and GNBs-Cur were estimated to be 31874 and 35332, respectively. The semiquantitative analysis of CLSM images also indicated the highest FL intensity after 4 h of endocytosis, which was similar to the flow cytometry (FC) results (Fig. 4C). These findings suggest that GNBs can serve as effective carriers for the delivery of Cur. As concluded from the data, the final performance of GNBs-Cur exhibited effective cellular uptake efficiency, which facilitated the therapeutic effect of the in vivo treatment.

Before evaluating the in vitro mild PTT/chemotherapy performance, the cytotoxicity of GNBs was evaluated. To demonstrate the synergistic effect of chemotherapy and mild PTT, cell viability after distinct treatments was investigated using the CCK-8 assay. For in vitro mild PTT, the survival rate of cells decreased with improved concentrations of GNBs, similar to the therapeutic effect in a dose-dependent manner when the laser was turned on or off (Fig. S8). For in vitro chemotherapy, cell viability was reduced as the concentration of Cur was increased from 0 to 20 μM (Fig. S9). In addition, cells treated with GNBs-Cur in the absence of laser irradiation demonstrated a moderate cell killing effect with 51 % viability under a Cur concentration of 20 μM. Mild PTT or chemotherapy alone did not lead to sufficient A549 cell killing ability. In contrast, a markedly augmented cell killing effect was observed for A549 cells treated with GNBs-Cur upon laser irradiation, leading to a survival rate of only 25 %, indicating a synergistic effect between chemotherapy and mild PTT. Furthermore, to further assess the synergistic antitumor efficacy of chemotherapy and mild PTT, A549 cells in various treatments were stained using the Calcein-AM/PI staining kit (Fig. 4E and F). Only green spots were observed in the PBS and NIR groups, while the GNBs + NIR showed a small number of red spots, implying that mild PPT alone did not have a desired antitumor effect. However, more red spots were observed in the GNBs-Cur group treated with laser radiation (GNBs-Cur + NIR), demonstrating the effective antitumor effect of chemotherapy and mild PTT synergistic therapy.

Additionally, FC was performed to investigate the death pattern of A549 cells after distinct treatments. The FC results indicated that the survival rates of A549 cells treated with NIR or GNBs + NIR were 88.4 % and 86.4 % (Fig. 4G). The apoptosis rates of the Cur and GNBs-Cur groups were 16 % and 23 %, respectively. After exposure to 1064 nm laser irradiation, the apoptosis rate induced by GNBs-Cur reached 30 %,

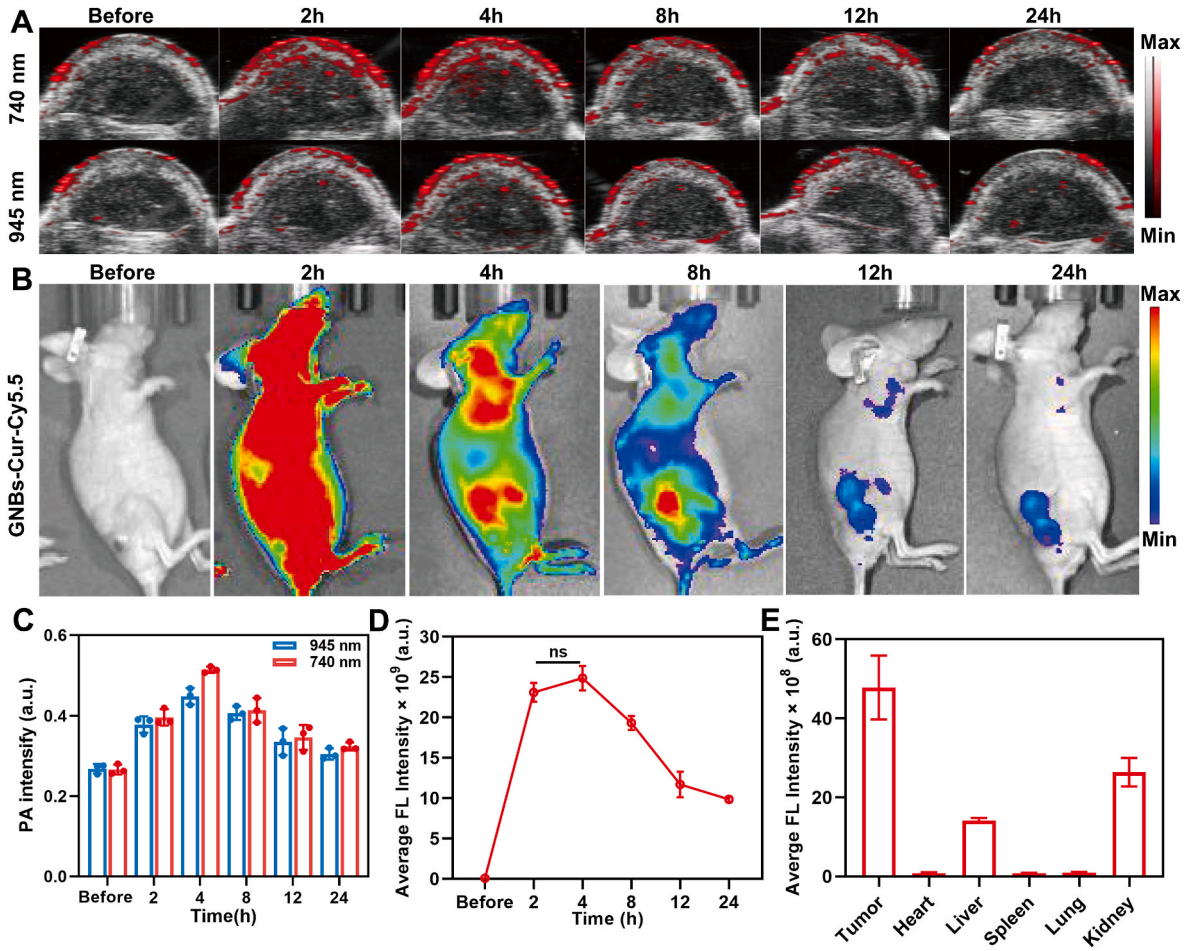

Fig. 6. In vivo FL and PA images of GNBs-Cur in A549-bearing mice. **(A)** In vivo PA images (λex = 740 nm and 945 nm) of mice before and after injection with GNBs-Cur. **(B)** FL images of the GNBs-Cur accumulation in tumors. **(C)** Quantitative PA intensity of tumors at distinct time points (n = 3). **(D)** Semiquantitative FL intensity of tumor site at different time points (n = 3). **(E)** FL intensity of major organs from GNBs-Cur-treated mice.

which was significantly higher than that triggered by other treatments. The highest apoptosis rate of GNBs-Cur nanoparticles under laser irradiation further demonstrated the effectiveness of chemotherapy and NIR-II-responsive mild PTT combination at the cellular level in vitro.

3.6. Mechanism of GNBs-Cur remodeling of the thermoresistant microenvironment

The therapeutic efficacy of mild PTT is limited by HSP90 expression and related anti-apoptotic pathways in A549 cells [46,47]. Based on the results of bioinformatic analysis, we hypothesized that GNBs-Cur could inhibit the high expression of HSP90 to remodel the thermoresistant microenvironment; thus, western blot was performed to investigate the mechanism of GNBs-Cur treatment. As shown in Fig. 5A–E and S10A–C, HSP90 expression was significantly downregulated in the presence of Cur compared to the PBS and mild PTT groups (GNBs + NIR). The GNBs-Cur + NIR group exhibited HSP90 expression that was approximately 2.2-fold lower than that of the cells in the PBS and GNBs + NIR groups. Correspondingly, the related client proteins (AKT, p-AKT, PI3K, and p-PI3K) were effectively blocked by the inhibition of HSP90 expression. The relative expression values of p-AKT and p-PI3K in A549 cells incubated with GNBs-Cur under laser irradiation were 0.51 and 0.49, respectively, which were much lower than those of the PBS groups (1.03 and 1.01, respectively). We also examined the levels of apoptosis-related proteins downstream (caspase 3) of the PI3K/AKT pathway. It is well known that caspase 3 is the major end-shedding enzyme in apoptosis and that it is autoclaved when the apoptosis is initiated [18]. Fig. 5A and D shows that caspase 3 expression was significantly reduced by 7.14-fold in the GNBs-Cur + NIR group compared to the PBS group. Thus, according to previous studies [48–51], we speculated that Cur could bind to HSP90, resulting in a decrease in HSP90 stability and its degradation via the proteasome pathway. Meanwhile, downregulation of HSP90 leads to impeded folding of client proteins such as AKT and PI3K (Fig. 5F). Collectively, these results indicated that GNBs-Cur with irradiation effectively inhibited the upregulation of HSP90 and its client proteins, while apoptosis of tumor cells was triggered by the synergistic effects of GNB-induced mild PTT and Cur-generated chemical damage and cell thermotolerance decrease.

3.7. Real-time PA/FL imaging

Before evaluating the therapeutic efficacy of GNBs-Cur in vivo, in vivo FL/PA imaging was performed in A549 tumor-bearing mice. Considering the robust and extensive near-infrared (NIR) absorption characteristics of GNBs-Cur, employing wavelengths of 740 nm and 945 nm can effectively leverage the optical properties of GNBs (Fig. S11). This approach enhances the informational content of photoacoustic signals, thereby improving the sensitivity and accuracy of imaging. Photoacoustic imaging were employed to elucidate the in vivo distribution of GNBs-Cur and to ascertain the optimal time window for administering mild PTT. After injecting GNBs-Cur, PA images were taken with 740 and 945 nm laser illumination at designated time intervals (2, 4, 8, 12, and 24 h), and PA images were also taken before

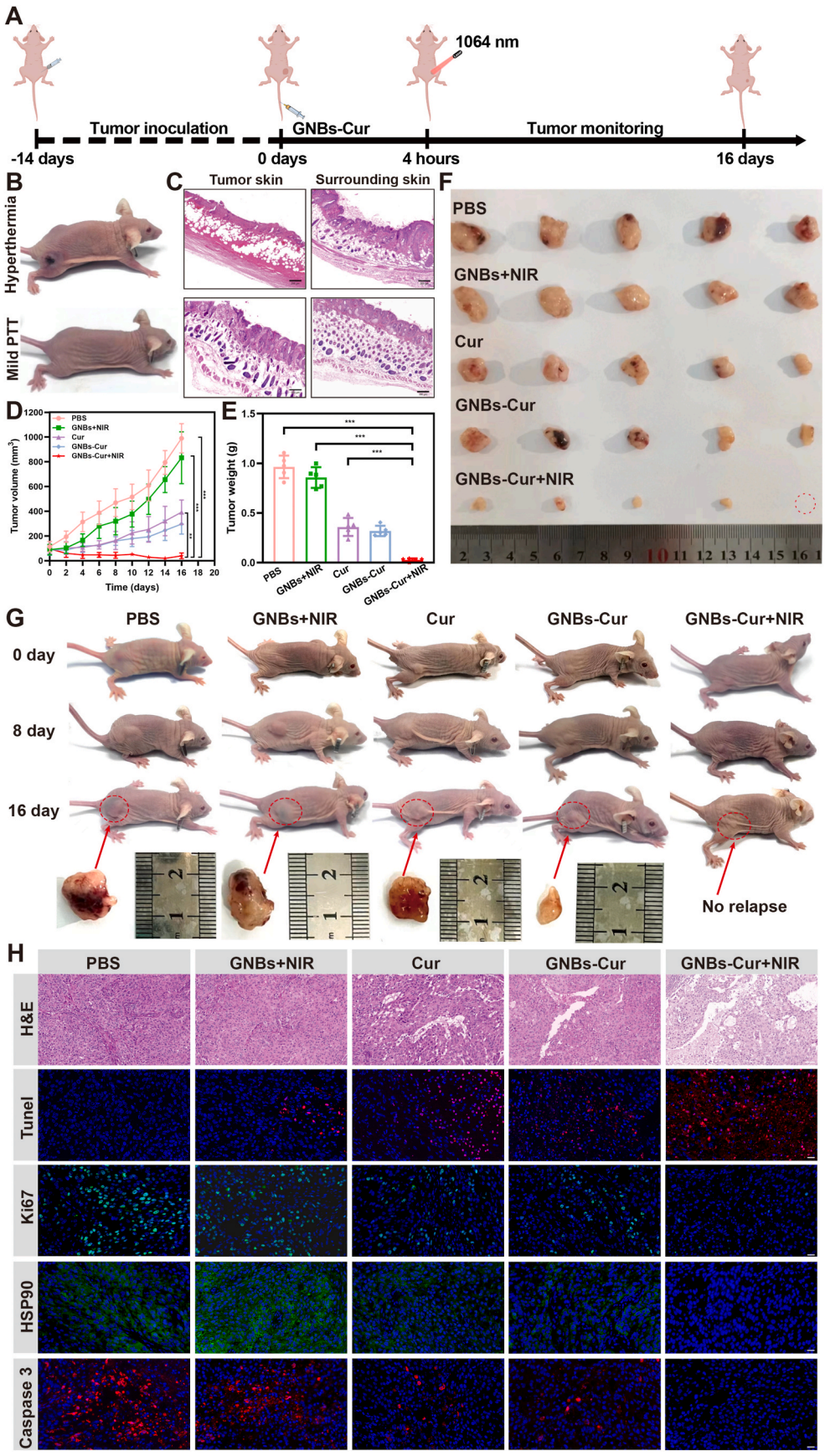

(caption on next page)

Fig. 7. In vivo synergistic mild PTT and chemotherapy of GNBs-Cur for NSCLC. **(A)** Schematic illustration of the GNBs-Cur therapy procedure in vivo. **(B, C)** H&E staining of skin (scale bar = 200 μm) and photographs of mice treated with GNBs-Cur with 1064 nm laser at 1 W cm^{-2} (mild PTT) and at 1.5 W cm^{-2} (hyperthermia). **(D)** Tumor growth curves of mice in various groups. **(E)** Tumor weights in various groups. Data are shown as the mean ± S.D (n = 5). **p < 0.01, ***p < 0.001. **(F)** Photographs of ex vivo tumors in different groups. (G) Representative photographs of mice and corresponding excised tumors on day 16 after different treatments. **(H)** H&E staining (scale bar = 50 μm), IF TUNEL, Ki67, HSP90, and caspase 3 staining of tumor sections in various groups (scale bar = 20 μm).

injection. As shown in Fig. 6A, the PA signal intensity of tumors was gradually enhanced over time and reached a maximum at 4 h, which was attributed to the accumulation of GNBs-Cur through the EPR effect. The semi-quantitative analysis showed that the average PA intensities under 740 nm and 945 nm laser illumination were approximately 0.514 and 0.448 a.u. at 4 h, respectively, which were 1.93 times and 1.67 times higher than those before injection (Fig. 6B). Meanwhile, we also performed whole-body FL imaging to investigate the in vivo biodistribution of GNBs-Cur. FL imaging was implemented at 2, 4, 8, 12, and 24 h post-injection. As illustrated in Fig. 6C and D, a duration of 4 h was identified as the optimal laser irradiation time for mild PTT to minimize potential side effects. At 24 h post injection, mice were sacrificed, and major organs were collected for biodistribution analysis. The FL images indicated that GNBs-Cur accumulated in the tumor (Fig. 6E and S12). Meanwhile, high FL intensities were observed in the liver and kidney, indicating that GNBs-Cur could be metabolized in vivo. The FL/PA imaging results revealed that laser irradiation of the tumor region was conducted at 4 h, which may achieve optimal mild PTT/chemotherapy efficacy.

3.8. *In vivo mild photothermal chemotherapy of GNBs-Cur*

Given the favorable efficacy of GNBs-Cur-mediated mild PTT combined with chemotherapy in inducing cell apoptosis, we further investigated whether a similar effect occurred in A549 tumor-bearing nude mice following the protocol shown in Fig. 7A. Initially, we examined the extent of damage inflicted on adjacent normal tissues by hyperthermia

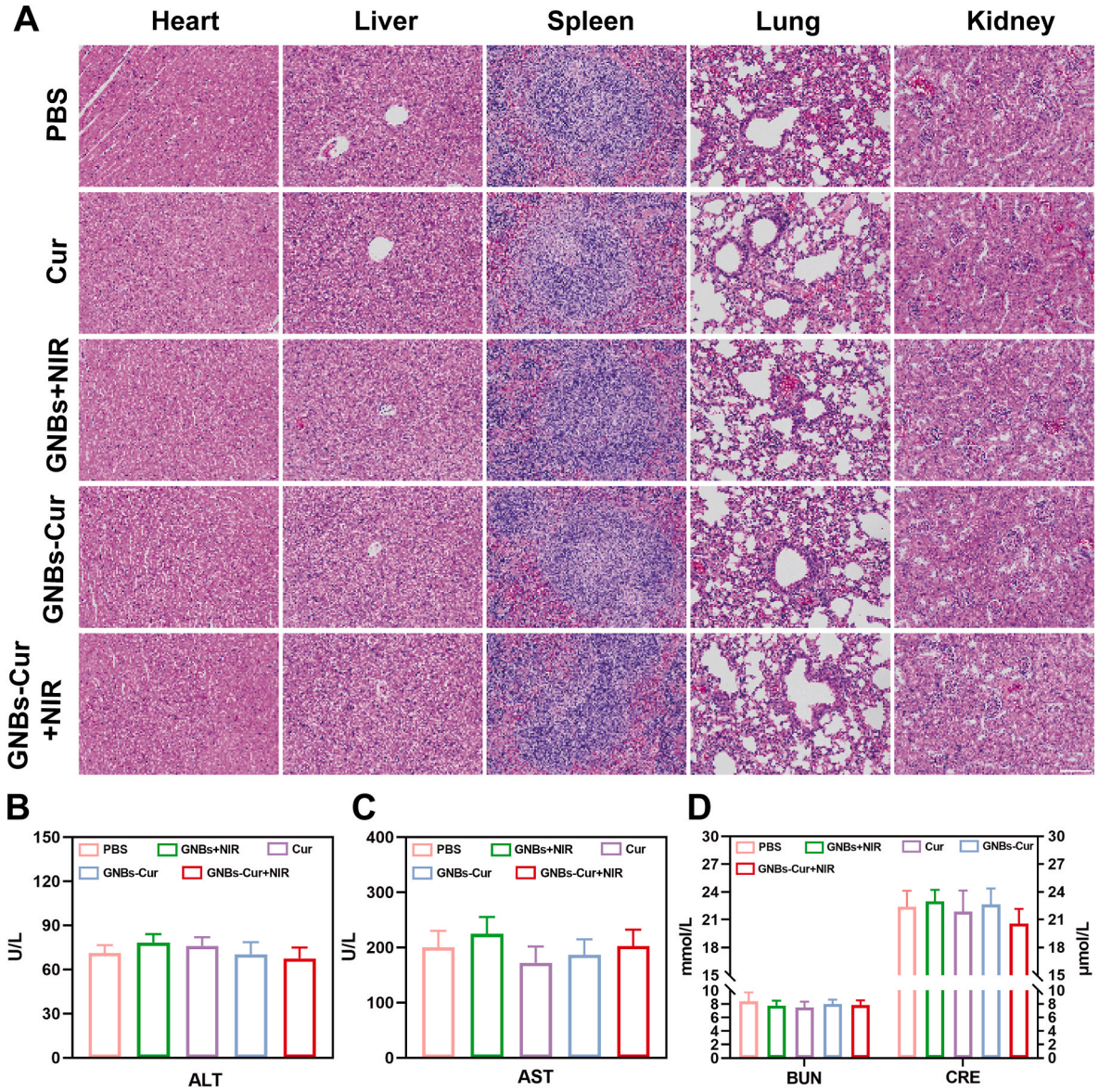

Fig. 8. Biosafety evaluation in vivo. **(A)** H&E levels of major organs (heart, liver, spleen, lung, and kidney) excised from mice treated with PBS, Cur, GNBs + NIR, GNBs-Cur, and GNBs-Cur + NIR (scale bar = 100 μm). **(B, C)** Serum levels of AST and ALT (liver function markers) in nude mice in different groups (n = 5). **(D)** Serum levels of BUN and CRE (kidney function markers) in nude mice in various groups (n = 5).

therapy and mild PTT. The maximum temperatures achieved in the tumors during mild PTT and hyperthermia therapy were 43 °C (1 W/cm^{-2}) and 58 °C (1.5 W/cm^{-2}), respectively (Fig. S13). Following intravenous injection of GNBs-Cur, H&E staining of the skin was performed on mice after irradiation using lasers. The results showed no significant inflammation or thermal damage in the tumor skin and surrounding normal tissues with mild PTT compared to conventional PTT, implying that mild PTT has better biocompatibility (Fig. 7B and C). The in vivo mild PTT/chemotherapy performance was subsequently evaluated, in which mice were randomly divided into five groups: PBS, GNBs + NIR, Cur, GNBs-Cur, and GNBs-Cur + NIR. We validated the antitumor performance by analyzing the volume, weight, and photograph of the extracted tumors (Fig. 7D–G). As shown in Fig. 7D and E, the volume and weight of tumors in the GNB + NIR group were consistent with those of the PBS group, indicating that the cytotoxicity of single mild PTT was slight. The tumor growth of the Cur and GNBs-Cur groups exhibited moderate inhibition, while the GNBs-Cur + NIR group achieved better tumor suppression owing to the excellent synergetic lung cancer mild PTT/chemotherapeutic regimen. Digital photographs of mice and ex vivo tumors revealed that the GNBs-Cur + NIR group had the smallest tumors compared to those in the other groups, further proving the therapeutic effect of GNBs-Cur + NIR (Fig. 7F and G). Throughout the treatment period, no significant difference in body weight was observed among the groups (Fig. S14).

To investigate the tumor inhibition mechanisms of GNBs-Cur, histological analysis of tumor slices was first performed at the end of treatment to observe pathological changes at the histological level (Fig. 7H). There was no significant organ damage in the PBS and GNBs + NIR groups through H&E staining, whereas the GNBs-Cur + NIR group exhibited severe tissue damage after treatment. TUNEL staining revealed that the number of red fluorescent dots increased remarkably in tumors of the GNBs-Cur + NIR group, indicating the presence of many apoptotic cells at the tumor site after GNBs-Cur + NIR treatment. Ki67 staining exhibited a weak green signal, indicating the potential of GNBs-Cur + NIR treatment to suppress tumor cell proliferation. To determine the mechanism of GNBs-Cur, immunofluorescence (IF) staining was used to evaluate the expression of HSP90 and caspase 3. The IF showed that HSP90 and caspase 3 were significantly downregulated in tumors of the GNBs-Cur + NIR group, thus inducing apoptosis of tumor cells by remolding the thermoresistant microenvironment and enhancing their sensitivity to chemotherapy. These results elucidate the excellent antitumor efficiency of GNBs-Cur-mediated synergistic mild PTT and chemotherapy.

3.9. Biosafety evaluation of GNBs-Cur

After subjecting mice to different treatments (including PBS, Cur, GNBs + NIR, GNBs-Cur, and GNBs-Cur + NIR), a comprehensive biotoxicity analysis was conducted to assess the biosafety of GNBs-Cur. The heart, liver, spleen, lung, and kidneys were stained with H&E dye for histopathological examination. As shown in Fig. 8A, compared to the PBS group, no significant pathological damage was observed in the major organs of the GNBs-Cur and GNBs-Cur + NIR groups, demonstrating the high biocompatibility of NIR-II responsive GNBs-Cur. Furthermore, the biochemical indices of blood indicated that, upon GNBs-Cur + NIR treatment, either the hepatic function indices (AST and ALT) or the renal function indices (CREA and UREA) remained within the normal range and exhibited no obvious difference compared to those of the PBS group (Fig. 8B–D). These findings confirmed the excellent biological safety and biocompatibility of NIR-II-responsive GNBs-Cur.

4. Conclusion

Overexpression of HSP90 in tumor cells can shape the thermoresistant microenvironment and activate the antiapoptotic pathway during treatment, thereby reducing the therapeutic efficacy. Nanomaterials combined with bioinformatics enable the design of nanomedicines that effectively block the HSP90 pathway and related molecular chaperone expression. In summary, we successfully developed an NIR-II responsive nanoplatform (GNBs-Cur) to enhance mild PTT and chemotherapy for NSCLC. Based on computational simulations and protein structure prediction, the strength of drug-HSP90 interactions was investigated, and strong binding was observed between Cur and HSP90. We predicted that GNBs-Cur could effectively inhibit the upregulation of HSP90 and block the intracellular anti-apoptotic pathway to enhance apoptosis in tumor cells via network pharmacology. We further demonstrated that GNBs-Cur downregulate HSP90 in tumor cells under laser exposure, resulting in increased sensitivity of tumor cells to heat stress and drugs. After intravenous injection into the body, PA-imaging-guided GNBs-Cur exhibited good tumor accumulation behavior and significant tumor suppression on the basis of a combination of mild PTT and chemotherapy. Overall, our findings not only emphasize the importance of bioinformatics in guiding nanomedicine design but also provide new directions for developing multimodal synergistic therapies against NSCLC.

CRediT authorship contribution statement

Zhenying Diao: Writing – review & editing, Writing – original draft, Methodology, Data curation, Conceptualization. **Youcheng Liang:** Writing – review & editing, Writing – original draft, Methodology, Data curation. **Yong Liu:** Writing – review & editing, Writing – original draft, Methodology, Conceptualization. **Dou Zhang:** Methodology, Conceptualization. **Long Qiu:** Visualization, Validation, Investigation. **Jianbo Sun:** Visualization, Project administration, Formal analysis. **Qiaoyou Lu:** Writing – review & editing, Writing – original draft, Visualization, Supervision, Funding acquisition. **Yanlei Liu:** Writing – review & editing, Validation, Supervision, Software, Methodology. **Daxiang Cui:** Writing – review & editing, Validation, Supervision, Project administration, Funding acquisition, Conceptualization. **Ting Yin:** Writing – review & editing, Writing – original draft, Visualization, Supervision, Funding acquisition.

Declaration of competing interest

All the authors declare no competing interests.

Acknowledgement

This work was supported by Natural Science Foundation of Guangdong Province, China (2024A1515030063, 2022A1515011337), Guangdong Province Universities and Colleges Characteristic Innovation (2021KTSCX036), Traditional Chinese Medicine Research Project of Guangdong Province Traditional Chinese Medicine Bureau (20221206), Discipline Construction Project of Guangdong Medical University (4SG24015G), Guangdong Students' Platform for innovation and entrepreneurship training program (S202410571110), Construction Project of Nano Technology and Application Engineering Research Center of Guangdong Medical University (4SG24179G) and Funds for PHD researchers of Guangdong Medical University in 2024.

Appendix A. Supplementary data

Supplementary data to this article can be found online at https://doi.org/10.1016/j.mtbio.2025.101541.

Data availability

Data will be made available on request.

References

[1] C. Xu, K. Pu, Second near-infrared photothermal materials for combinational nanotheranostics, Chem. Soc. Rev. 50 (2021) 1111–1137, https://doi.org/10.1039/D0CS00664E.

[2] X. Zhang, X. Si, Y. Wang, Y. Li, C. Xu, H. Tian, Polymerization and coordination synergistically constructed photothermal agents for macrophages-mediated tumor targeting diagnosis and therapy, Biomaterials 264 (2021) 120382, https://doi.org/10.1016/j.biomaterials.2020.120382.

[3] Y. Liu, P. Bhattarai, Z. Dai, X. Chen, Photothermal therapy and photoacoustic imaging via nanotheranostics in fighting cancer, Chem. Soc. Rev. 48 (2019) 2053–2108, https://doi.org/10.1039/C8CS00618K.

[4] J. Chen, C. Ning, Z. Zhou, P. Yu, Y. Zhu, G. Tan, C. Mao, Nanomaterials as photothermal therapeutic agents, Prog. Mater. Sci. 99 (2019) 1–26, https://doi.org/10.1016/j.pmatsci.2018.07.005.

[5] Q. Yu, J. Zhou, H. Wang, Y. Liu, H. Zhou, B. Kang, H.Y. Chen, J.J. Xu, A multiple-response cascade nanoreactor for starvation and deep catalysis chemodynamic assisted near-infrared-II mild photothermal therapy, Chem Biomed Imaging 1 (2023) 242–250, https://doi.org/10.1021/cbmi.2c00003.

[6] N. Sharma, W. Mohammad, X. Le Guével, A. Shanavas, Gold nanoclusters as high resolution NIR-II theranostic agents, Chem Biomed Imaging. 2 (2024) 462–480, https://doi.org/10.1021/cbmi.4c00021.

[7] N. Li, F. Shen, Z. Cai, W. Pan, Y. Yin, X. Deng, X. Zhang, J.O. Machuki, Y. Yu, D. Yang, et al., Target-induced core-satellite nanostructure assembly strategy for dual-signal-on fluorescence imaging and Raman quantification of intracellular MicroRNA guided photothermal therapy, Small 16 (2020) e2005511, https://doi.org/10.1002/smll.202005511.

[8] Z. Sun, W. Chen, D. Huang, C. Jiang, L. Lu, A mitochondria targeted cascade reaction nanosystem for improved therapeutic effect by overcoming cellular resistance, Biomater. Sci. 10 (2022) 5947–5955, https://doi.org/10.1039/D2BM00956K.

[9] C. Li, E. Mei, C. Chen, Y. Li, B. Nugasur, L. Hou, X. Ding, M. Hu, Y. Zhang, Z. Su, et al., Gold-nanobipyramid-based nanotheranostics for dual-modality imaging-guided phototherapy, ACS Appl. Mater. Interfaces 12 (2020) 12541–12548, https://doi.org/10.1021/acsami.0c00112.

[10] X. Zhang, C. Zhang, N. Li, W. Pan, M. Fu, J. Ong'achwa Machuki, K. Ge, Z. Liu, F. Gao, Gold-bipyramid-based nanothernostics: FRET-mediated protein-specific sialylation visualization and oxygen-augmenting phototherapy against hypoxic tumor, Anal. Chem. 93 (2021) 12103–12115, https://doi.org/10.1021/acs.analchem.1c02625.

[11] C. Yin, X. Li, Y. Wang, Y. Liang, S. Zhou, P. Zhao, C.S. Lee, Q. Fan, W. Huang, Organic semiconducting macromolecular dyes for NIR-II photoacoustic imaging and photothermal therapy, Adv. Funct. Mater. 31 (2021) 2104650, https://doi.org/10.1002/adfm.202104650.

[12] Q. Miao, K. Pu, Organic semiconducting agents for deep-tissue molecular imaging: second near-infrared fluorescence, self-luminescence, and photoacoustics, Adv Mater 30 (2018) e1801778, https://doi.org/10.1002/adma.201801778.

[13] Y. Chen, S. Chen, H. Yu, Y. Wang, M. Cui, P. Wang, P. Sun, M. Ji, D-A type NIR-II organic molecules: strategies for the enhancement fluorescence brightness and applications in NIR-II fluorescence imaging-navigated photothermal therapy, Adv Healthc Mater 11 (2022) e2201158, https://doi.org/10.1002/adhm.202201158.

[14] Y. Dai, H. Zhao, K. He, W. Du, Y. Kong, Z. Wang, M. Li, Q. Shen, P. Sun, Q. Fan, NIR-II excitation phototheranostic nanomedicine for fluorescence/photoacoustic tumor imaging and targeted photothermal-photonic thermodynamic therapy, Small 17 (2021) e2102527, https://doi.org/10.1002/smll.202102527.

[15] K. Yang, S.J. Zhao, B.L. Li, B.H. Wang, M.H. Lan, X.Z. Song, Low temperature photothermal therapy: advances and perspectives, Coord. Chem. Rev. 454 (2022) 10–8545, https://doi.org/10.1016/j.ccr.2021.214330.

[16] G. Ma, Z. Liu, C. Zhu, H. Chen, R.T.K. Kwok, P. Zhang, B.Z. Tang, L. Cai, P. Gong, H_2O_2 -responsive NIR-II AIE nanobomb for carbon monoxide boosting low-temperature photothermal therapy, Angew Chem Int Ed Engl. 61 (2022) e202207213, https://doi.org/10.1002/anie.202207213.

[17] H. Chen, B.B. Ding, J. Tan, P. Zheng, Z.Y. Cheng, P.A. Ma, J. Lin, Palladium hydride nanourchins with amplified photothermal therapeutic effects through controlled hydrogen release and antigen-assisted immune activation, Chem. Eng. J. 442 (2022) 1385–8947, https://doi.org/10.1016/j.cej.2022.136296.

[18] L. Yang, X. Hou, Y. Zhang, D. Wang, J. Liu, F. Huang, J. Liu, NIR-activated self-sensitized polymeric micelles for enhanced cancer chemo-photothermal therapy, J Control Release 339 (2021) 114–129, https://doi.org/10.1016/j.jconrel.2021.09.017.

[19] T.Y. Lin, W. Guo, Q. Long, A. Ma, Q. Liu, H. Zhang, Y. Huang, S. Chandrasekaran, C. Pan, K.S. Lam, et al., HSP90 inhibitor encapsulated photo-theranostic nanoparticles for synergistic combination cancer therapy, Theranostics 6 (2016) 1324–1335. https://www.thno.org/v06p1324.htm.

[20] X. Niu, Y. Zhu, C. Ding, J. Ma, P. Wei, Y. Lin, W. Fang, Q. He, C. Li, J. Cheng, et al., Dual-active center AgFeCu nanocatalyst for tumor destruction via self-catalytically enhanced mild photothermal therapy, Adv. Funct. Mater. 33 (2023) 2306778, https://doi.org/10.1002/adfm.202306778.

[21] L. Wang, Y. Yu, D. Wei, L. Zhang, X. Zhang, G. Zhang, D. Ding, H. Xiao, D. Zhang, A systematic strategy of combinational blow for overcoming cascade drug resistance via NIR-light-triggered hyperthermia, Adv Mater 33 (2021) e2100599, https://doi.org/10.1002/adma.202100599.

[22] P. Zhang, D. Zhang, W. Zhou, L. Wang, B. Wang, T. Zhang, S. Li, Network pharmacology: towards the artificial intelligence-based precision traditional Chinese medicine, Brief Bioinform 25 (2023), https://doi.org/10.1093/bib/bbad518 bbad518.

[23] K. Zhu, Y. Yao, K. Wang, F. Shao, Z. Zhu, Y. Song, Z. Zhou, D. Jiang, X. Lan, C. Qin, Berberin sustained-release nanoparticles were enriched in infarcted rat myocardium and resolved inflammation, J Nanobiotechnology 21 (2023) 33, https://doi.org/10.1186/s12951-023-01790-w.

[24] Y. Liu, M. Hou, Z. Pan, X. Tian, Z. Zhao, T. Liu, H. Yang, Q. Shi, X. Chen, Y. Zhang, F. He, X. Zhu, Arctiin-reinforced antioxidant microcarrier antagonizes osteoarthritis progression, J Nanobiotechnology 20 (2022) 303, https://doi.org/10.1186/s12951-022-01505-7.

[25] K. Rahme, N. Dagher, Chemistry routes for copolymer synthesis containing PEG for targeting, imaging, and drug delivery purposes, Pharmaceutics 11 (2019) 327, https://doi.org/10.3390/pharmaceutics11070327.

[26] Z. Min, Z. Hengrui, F. Jie, Z. Yunlong, W. Bailiang, Synergistic chemotherapy, physiotherapy and photothermal therapy against bacterial and biofilms infections through construction of chiral glutamic acid functionalized gold nanobipyramids, Chem. Eng. J. 393 (2020) 1385–8947, https://doi.org/10.1016/j.cej.2020.124778.

[27] A.S. Shehab, E.K. Riham, P. Digambara, Curcumin mediated PEG thiol acid conjugated gold nanoparticles for the determination of melamine, Microchem. J. 153 (2020) 26–265X, https://doi.org/10.1016/j.microc.2019.104382.

[28] N.M. Vaibhavkumar, G. Nirav, V.R. Jigneshkumar, K.S. Rakesh, B. Hirakendu, K. K. Suresh, Ligand chemistry of gold, silver and copper nanoparticles for visual read-out assay of pesticides: a review, TrAC, Trends Anal. Chem. 153 (2022) 165–9936, https://doi.org/10.1016/j.trac.2022.116607.

[29] P.S. Sadalage, R.V. Patil, D.V. Havaldar, S.S. Gavade, A.C. Santos, K.D. Pawar, Optimally biosynthesized, PEGylated gold nanoparticles functionalized with quercetin and camptothecin enhance potential anti-inflammatory, anti-cancer and anti-angiogenic activities, J Nanobiotechnology 19 (2021) 84, https://doi.org/10.1186/s12951-021-00836-1.

[30] D. Yan, G. Zheng, C. Wang, Z. Chen, T. Mao, J. Gao, Y. Yan, X. Chen, X. Ji, J. Yu, et al., Hit 2.0: an enhanced platform for herbal ingredients' targets, Nucleic Acids Res. 50 (2022) D1238–D1243, https://doi.org/10.1093/nar/gkab1011.

[31] Y. Zhou, Y. Zhang, D. Zhao, X. Yu, X. Shen, Y. Zhou, S. Wang, Y. Qiu, Y. Chen, F. Zhu, TTD: therapeutic Target Database describing target druggability information, Nucleic Acids Res. 52 (2024) D1465–D1477, https://doi.org/10.1093/nar/gkad751.

[32] A. Daina, O. Michielin, V. Zoete, SwissADME: a free web tool to evaluate pharmacokinetics, drug-likeness and medicinal chemistry friendliness of small molecules, Sci. Rep. 7 (2017) 42717, https://doi.org/10.1038/srep42717.

[33] O. Trott, A.J. Olson, AutoDock Vina: improving the speed and accuracy of docking with a new scoring function, efficient optimization, and multithreading, J. Comput. Chem. 31 (2010) 455–461, https://doi.org/10.1002/jcc.21334.

[34] Y. Wu, F. Zhang, K. Yang, S. Fang, D. Bu, H. Li, L. Sun, H. Hu, K. Gao, W. Wang, et al., SymMap: an integrative database of traditional Chinese medicine enhanced by symptom mapping, Nucleic Acids Res. 47 (2019) D1110–D1117, https://doi.org/10.1093/nar/gky1021.

[35] J. Ru, P. Li, J. Wang, W. Zhou, B. Li, C. Huang, P. Li, Z. Guo, W. Tao, Y. Yang, et al., TCMSP: a database of systems pharmacology for drug discovery from herbal medicines, J Cheminform 6 (2014) 13, https://doi.org/10.1186/1758-2946-6-13.

[36] A. Daina, O. Michielin, V. Zoete, SwissTargetPrediction: updated data and new features for efficient prediction of protein targets of small molecules, Nucleic Acids Res. 47 (2019) W357–W364, https://doi.org/10.1093/nar/gkz382.

[37] D. Szklarczyk, J.H. Morris, H. Cook, M. Kuhn, S. Wyder, M. Simonovic, A. Santos, N.T. Doncheva, A. Roth, P. Bork, et al., The STRING database in 2017: quality-controlled protein-protein association networks, made broadly accessible, Nucleic Acids Res. 45 (2017) D362–D368, https://doi.org/10.1093/nar/gkw937.

[38] G.D. Bader, C.W. Hogue, An automated method for finding molecular complexes in large protein interaction networks, BMC Bioinf. 4 (2003) 2, https://doi.org/10.1186/1471-2105-4-2.

[39] Y. Zhou, B. Zhou, L. Pache, M. Chang, A.H. Khodabakhshi, O. Tanaseichuk, C. Benner, S.K. Chanda, Metascape provides a biologist-oriented resource for the analysis of systems-level datasets, Nat. Commun. 10 (2019) 1523, https://doi.org/10.1038/s41467-019-09234-6.

[40] M.E. Ritchie, B. Phipson, D. Wu, Y. Hu, C.W. Law, W. Shi, G.K. Smyth, Limma powers differential expression analyses for RNA-sequencing and microarray studies, Nucleic Acids Res. 43 (2015) e47, https://doi.org/10.1093/nar/gkv007.

[41] Z. Tang, C. Li, B. Kang, G. Gao, C. Li, Z. Zhang, GEPIA: a web server for cancer and normal gene expression profiling and interactive analyses, Nucleic Acids Res. 45 (2017) W98–W102, https://doi.org/10.1093/nar/gkx247.

[42] Y. Liu, Z. Li, Z. Yin, H. Zhang, Y. Gao, G. Huo, A. Wu, L. Zeng, Amplified photoacoustic signal and enhanced photothermal conversion of polydopamine-coated gold nanobipyramids for phototheranostics and synergistic chemotherapy, ACS Appl. Mater. Interfaces 12 (2020) 14866–14875.

[43] M.E. Youssef, S. Cavalu, A.M. Hasan, G. Yahya, M.A. Abd-Eldayem, S. Saber, Role of ganetespib, an HSP90 inhibitor, in cancer therapy: from molecular mechanisms to clinical practice, Int. J. Mol. Sci. 24 (2023) 5014, https://doi.org/10.3390/ijms24055014.

[44] A. Sánchez-Iglesias, N. Winckelmans, T. Altantzis, S. Bals, M. Grzelczak, L.M. Liz-Marzán, High-yield seeded growth of monodisperse pentatwinned gold nanoparticles through thermally induced seed twinning, J. Am. Chem. Soc. 139 (2017) 107–110, https://doi.org/10.1021/jacs.6b12143.

[45] C. Li, E. Mei, C. Chen, Y. Li, B. Nugasur, L. Hou, X. Ding, M. Hu, Y. Zhang, Z. Su, et al., Gold-nanobipyramid-based nanotheranostics for dual-modality imaging-guided phototherapy, ACS Appl. Mater. Interfaces 12 (2020) 12541–12548, https://doi.org/10.1021/acsami.0c00112.

[46] T. Shimamura, G.I. Shapiro, Heat shock protein 90 inhibition in lung cancer, J. Thorac. Oncol. 3 (2008) S152–S159, https://doi.org/10.1097/JTO.0b013e318174ea3a.

[47] S.S. Patel, A. Acharya, R.S. Ray, R. Agrawal, R. Raghuwanshi, P. Jain, Cellular and molecular mechanisms of curcumin in prevention and treatment of disease, Crit. Rev. Food Sci. Nutr. 60 (2020) 887–939, https://doi.org/10.1080/10408398.2018.1552244.

[48] A.A.A. Abdelmoaty, P. Zhang, W. Lin, Y.J. Fan, S.N. Ye, J.H. Xu, C0818, a novel curcumin derivative, induces ROS-dependent cytotoxicity in human hepatocellular carcinoma cells in vitro via disruption of Hsp90 function, Acta Pharmacol. Sin. 43 (2022) 446–456, https://doi.org/10.1038/s41401-021-00642-3.

[49] D. Jiao, J. Wang, W. Lu, X. Tang, J. Chen, H. Mou, Q.Y. Chen, Curcumin inhibited HGF-induced EMT and angiogenesis through regulating c-Met dependent PI3K/Akt/mTOR signaling pathways in lung cancer, Mol Ther Oncolytics 3 (2016) 16018, https://doi.org/10.1038/mto.2016.18.

[50] C. Bai, J. Zhao, J. Su, J. Chen, X. Cui, M. Sun, X. Zhang, Curcumin induces mitochondrial apoptosis in human hepatoma cells through BCLAF1-mediated modulation of PI3K/AKT/GSK-3β signaling, Life Sci. 306 (2022) 120804, https://doi.org/10.1016/j.lfs.2022.120804.

[51] L. Hamzehzadeh, S.L. Atkin, M. Majeed, A.E. Butler, A. Sahebkar, The versatile role of curcumin in cancer prevention and treatment: a focus on PI3K/AKT pathway, J. Cell. Physiol. 233 (2018) 6530–6537, https://doi.org/10.1002/jcp.26620.